

RESEARCH ARTICLE

10.1002/2016JA023781

Key Points:

- Solar energetic particle precipitation can ionize and heat atmospheres of weakly magnetized planets
- A simulation was developed to predict atmospheric effects due to solar energetic particle precipitation into the Martian atmosphere
- Less atmospheric ionization occurs near crustal field anomalies than unmagnetized areas of Mars

Correspondence to:

R. D. Jolitz,
rebecca.jolitz@colorado.edu

Citation:

Jolitz, R. D., C. F. Dong, C. O. Lee, R. J. Lillis, D. A. Brain, S. M. Curry, S. Bougher, C. D. Parkinson, and B. M. Jakosky (2017), A Monte Carlo model of crustal field influences on solar energetic particle precipitation into the Martian atmosphere, *J. Geophys. Res. Space Physics*, 122, doi:10.1002/2016JA023781.

Received 23 DEC 2016

Accepted 25 APR 2017

Accepted article online 28 APR 2017

A Monte Carlo model of crustal field influences on solar energetic particle precipitation into the Martian atmosphere

R. D. Jolitz¹, C. F. Dong² , C. O. Lee³, R. J. Lillis³ , D. A. Brain¹ , S. M. Curry³ , S. Bougher⁴ , C. D. Parkinson⁴, and B. M. Jakosky¹ 

¹Laboratory for Atmospheric and Space Physics, University of Colorado Boulder, Boulder, Colorado, USA, ²Department of Astrophysical Sciences and Princeton Plasma Physics Laboratory, Princeton University, Princeton, New Jersey, USA, ³Space Sciences Laboratory, University of California, Berkeley, California, USA, ⁴Department of Atmospheric, Oceanic, and Space Sciences, University of Michigan, Ann Arbor, Michigan, USA

Abstract Solar energetic particles (SEPs) can precipitate directly into the atmospheres of weakly magnetized planets, causing increased ionization, heating, and altered neutral chemistry. However, strong localized crustal magnetism at Mars can deflect energetic charged particles and reduce precipitation. In order to quantify these effects, we have developed a model of proton transport and energy deposition in spatially varying magnetic fields, called Atmospheric Scattering of Protons and Energetic Neutrals. We benchmark the model's particle tracing algorithm, collisional physics, and heating rates, comparing against previously published work in the latter two cases. We find that energetic nonrelativistic protons precipitating in proximity to a crustal field anomaly will primarily deposit energy at either their stopping altitude or magnetic reflection altitude. We compared atmospheric ionization in the presence and absence of crustal magnetic fields at 50°S and 182°E during the peak flux of the 29 October 2003 "Halloween storm" SEP event. The presence of crustal magnetic fields reduced total ionization by ~30% but caused ionization to occur over a wider geographic area.

1. Introduction

Solar energetic particles (SEPs) are charged particles accelerated by the moving shock source ahead of a coronal mass ejection or by the local shock source at the solar flare site. They primarily consist of protons and electrons with energies from a few keV to up to several GeV. SEPs that precipitate into planetary atmospheres can have a substantial effect on ionospheric and neutral chemistry. In the terrestrial atmosphere, precipitating SEPs are known to cause heating, ionospheric outflow, and increased atmospheric ionization [Moore *et al.*, 1999; Usoskin *et al.*, 2009]. This in turn leads to enhanced electrical conductivity in the atmosphere, changes in lower atmosphere electrochemistry such as increased ozone concentrations via hydroxyl ion formation, and formation of aerosol particles between altitudes of 10 and 25 km [Kokorowski *et al.*, 2006; Damiani *et al.*, 2010; Mironova and Usoskin, 2014]. However, all of these effects are typically confined to the poles, as Earth's strong global magnetic field shields equatorial latitudes from energetic particles [Mironova *et al.*, 2015].

Mars, on the other hand, lacks a strong intrinsic magnetic field. Charged particles can precipitate into the atmosphere if they are accelerated past the compressed magnetic fields of the magnetosheath and bow shock formed by solar wind plasma draping over the dayside ionosphere [Acuña *et al.*, 2001]. Unlike solar wind particles, SEPs are mostly unaffected by this barrier. Phobos-2 measurements showed energetic particle fluxes recorded during a SEP event crossed the region without substantial change [McKenna-Lawlor *et al.*, 1998]. Subsequent modeling found that the barrier does not attenuate SEP protons with energies greater than 50 keV [Leblanc *et al.*, 2002].

There are two main obstacles to SEP entry into the atmosphere. The first is physical obstruction by the planet or "shadowing," which most strongly affects extremely energetic (>1 MeV) SEPs that are not significantly influenced by magnetic fields. Measurements from Mars Odyssey found that a combination of planetary shadowing, anisotropy of SEPs, and detector field of view caused orbital modulations of 20–200 MeV SEPs [Luhmann *et al.*, 2007]. The second obstacle is the localized crustal magnetic anomalies in the southern hemisphere that present strong magnetic fields capable of reflecting incident SEPs [Acuña *et al.*, 2001]. Prior

modeling studies on crustal anomaly influences on SEP fluxes suggest that the strongest field anomalies can attenuate SEP fluxes by over 50% at altitudes of 200 km [Leblanc *et al.*, 2002].

Compared to Earth, information on the atmospheric effects caused by SEP precipitation is relatively limited. Up until the Mars Atmosphere and Volatile Evolution (MAVEN) spacecraft's arrival at Mars, evidence of SEP precipitation was inferred from indirect observations during SEP events. SEP fluxes were determined by using background count rates in plasma analyzers as proxies for 20–100 MeV protons [Delory *et al.*, 2012; Futaana *et al.*, 2008]. Radar ground reflections observed by the Mars Advanced Radar for Subsurface and Ionospheric Sounding (MARSIS) instrument on Mars Express disappeared during SEP events, suggesting that SEP precipitation increased ionization [Morgan *et al.*, 2008; Espley *et al.*, 2007]. The Electron Reflectometer on Mars Global Surveyor measured increased upward fluxes of superthermal electrons linked to SEP events [Lillis *et al.*, 2012]. However, further analysis of radio occultation data during periods of high SEP activity only found small increases of electron density below altitudes of 100 km in four out of six SEP events and no increase in electron densities between altitudes of 100 and 200 km in all six events [Ulusen *et al.*, 2012]. SEP events were linked to ionization and electron production, but the exact mechanism remained unknown.

In 2014, MAVEN arrived at Mars carrying a suite of instruments designed to study the upper atmosphere and plasma environment, including a detector called solar energetic particle, or SEP, to directly monitor SEPs. The SEP instrument has been used to further characterize the near-Mars energetic particle environment. Measurements of anisotropic high-energy (>200 keV) SEP flux attenuation have confirmed Mars Odyssey observations of planetary shadowing. SEP has also observed complex low-energy shadowing governed by local magnetic field geometry [Lillis *et al.*, 2016]. The SEP instrument has also made measurements of SEP electrons and ions during solar flare and coronal mass ejection events [Lee *et al.*, 2017]. Coincident measurements of SEPs and atmospheric emission have led to the discovery of SEP electron-linked diffuse aurora [Schneider *et al.*, 2015].

SEP events are frequently coincident with changes in solar X-ray and extreme ultraviolet fluxes. Modeling studies can decouple these changes and isolate the causation of atmospheric effects like electron production and aurora.

SEP precipitation has been previously modeled using approximations. Leblanc *et al.* [2002] used a 1-D stopping-and-range-of-ions-in-matter (SRIM) model to calculate the total heating by SEPs in the atmosphere between altitudes of 80 and 170 km. Their model predicted SEP heating rates that were less than a tenth of heating rates due to solar ultraviolet fluxes, meaning SEP precipitation only increased atmospheric heating by ~30%. Sheel *et al.* [2012] used a stopping approximation that assumed all energy is deposited at a fixed altitude for a specific SEP energy. Once they predicted the total energy deposited for each trace species in the atmosphere, they determined ion densities by assuming an ion-electron pair is produced for every 35 eV deposited. They predicted that electron densities could reach 3000 cm^{-3} at 80 km during a SEP event that was 100 times weaker than the total flux measured during the 29 September 1989 SEP event, which would be sufficient to cause the MARSIS radar reflection disappearance. These approaches are mutually exclusive, as Sheel *et al.* [2012] assume that SEP energy deposition is solely imparted to ionization and Leblanc *et al.* [2002] assume that SEP energy deposition is imparted either to heating or electronic excitation.

SEP transport to the surface has also been modeled to predict the surface radiation environment during an event. Leblanc *et al.* [2002] estimate that only protons with energies greater than 83 MeV can make it to the surface. Because only extremely energetic particles can reach the surface, surface flux models need to account for nuclear processes. Planetocosmics and HZETRN (High-charge (Z) and Energy TRANsport) are two such models [Desorgher *et al.*, 2005; Norman *et al.*, 2013; Gronoff *et al.*, 2011]. Both models are in close agreement, predicting ionization rates of $\sim 1000\text{--}2000 \text{ cm}^{-3} \text{ s}^{-1}$ below 60 km during the 29 September 1989 SEP event [Gronoff *et al.*, 2015].

Existing models of SEP energy deposition do not account for differential energy deposition into heating, excitation, ionization, and charge transfer like the model presented in Kallio and Barabash [2001]. Others do not consider possible effects caused by proton gyromotion in crustal magnetic anomalies.

In this work, a three-dimensional Monte Carlo model of SEP precipitation called Atmospheric Scattering of Protons and Energetic Neutrals (ASPEN) is introduced to track transport and energy deposition of SEP protons in the Martian atmosphere. We will present a verification of tracing particle motion in magnetic fields and

validation of collision modeling. We will next discuss transport processes as a function of SEP proton energy, focusing on influences by crustal fields. Finally, we will use the ASPEN model results to predict ionization altitude profiles, maps, and secondary electron spectra during a specific SEP event.

2. Model Description

ASPEN uses Monte Carlo methods to predict energy deposition into a planetary atmosphere via charged particles, accounting for both particle motion in three-dimensional inhomogeneous electromagnetic fields and collisions with neutral molecules in the atmosphere. While existing GEANT4-based models like Planetocosmics are capable of this, we did not use them because we did not require their in-depth modeling of relativistic effects such as bremsstrahlung. ASPEN steps an incident particle through a planetary atmosphere and electromagnetic field until the calculated likelihood of collision along its path exceeds a randomly chosen collision probability. When that occurs, the consequences of the collision are determined (e.g., energy imparted to the atmosphere), and the particle begins stepping again until the particle energy falls below a given energy threshold or the particle exits the simulation boundaries.

The model has three key assumptions. First, neutral atmospheric molecules are stationary relative to each simulated particle. Second, simulated charged particles never interact with other charged particles. These assumptions restrict ASPEN to operating in altitudes where the density of simulated charged particles does not exceed the density of neutral targets, e.g., below 500 km. Third, electromagnetic fields and atmospheric densities do not temporally vary over the lifetime of a simulated particle.

To study atmospheric effects due to precipitating SEPs near crustal field anomalies, protons with energies up to 5 MeV are simulated and allowed to scatter between the altitudes of 70 km and 500 km. We focused on SEPs with energies below 5 MeV since they were most likely to be affected by crustal magnetic fields. By approximating the likelihood of an elastic collision as the ratio of the elastic cross section to the total cross section, we assumed that protons with energies that fall below 10 eV are no longer traced and are assumed to be thermalized, as a 10 eV proton has a 99.989% chance of imparting its energy to heat.

2.1. Model Dynamics

Individual protons are traced and allowed to collide with the atmosphere until they leave the preset altitude range or fall below the energy threshold. Each has an assigned fixed three-dimensional trajectory and location. They move according to the Lorentz force equation for a particle of charge q and mass m with position \vec{s} and velocity \vec{v} :

$$m \frac{d\vec{v}}{dt} = q \left(\vec{v} \times \vec{B}(\vec{s}) + \vec{E}(\vec{s}) \right)$$

A fourth-order Runge-Kutta method is used to solve this differential equation and approximate the change in velocity ($d\vec{v}$) and position ($d\vec{s}$) after elapsed time (dt). By repeatedly solving this equation using a time step dt , ASPEN determines a charged particle's Lorentz path.

To ensure the time step traces fine particle motion in complex field configurations, dt is set equal to $d/|\vec{v}|$ where \vec{v} is the particle's velocity and d is a spatial step length. Using a step length that is less than half of the shortest simulated proton's gyroradius in the strongest crustal fields ensures that the simulation correctly predicts gyromotion by all simulated protons. The lowest-energy particle simulated in this study is a 1 keV proton, which has a gyroradius of 5.9 km at the greatest magnetic field value (0.7 μ T) in the multifluid magnetohydrodynamics (MF-MHD) magnetic field mesh. Thus, we require that step length d does not exceed 1 km.

The step length d is also constrained by the distance between collisions. While particle motion is deterministic, particle collisions with the atmosphere are stochastic. The probability of a projectile colliding with a stationary target is random. However, a particle is more likely to collide if it travels in a denser medium or has a higher interaction cross-section area with a target. When applied to a particle beam of intensity I , this relation is known as Beer's law:

$$dI = -n\sigma dI$$

where n is the density of scattering targets, σ is the cross-sectional area presented by each scattering target, I is the beam intensity, and dl is the distance over which a beam attenuates. Following an approach for electron-neutral collisions from *Lillis et al.* [2008], we solved Beer's law for intensity and set the collision probability equal to the ratio of attenuated beam intensity to the initial beam intensity. For a particle traveling distance l and encountering N atmospheric species with spatially varying densities, this gives a probability of scattering of

$$P(l, U) = \exp \left[- \sum_i^N \int_0^l \sigma_i(U(l')) n_i(l') dl' \right]$$

where $\sigma_i(U(l'))$ is the cross section presented to a proton with energy $U(l')$ and $n_i(l')$ is the number density of the i th atmospheric neutral species encountered by the proton after traveling distance l' between 0 and l . By choosing a random probability for the left-hand side of the equation, we can use the equation to determine the distance l a particle travels before colliding, which is effectively a weighted random number. Because atmospheric densities and cross sections for each species may vary along a particle's path (i.e., along a curving path in magnetic field), we cannot directly solve this equation to find distance l for a random collision probability P . Instead, ASPEN implicitly solves for distance l between collisions by selecting a random number between 0 and 1 and incrementally moving the particle by dl' until the calculated probability of scatter exceeds the random probability on the left-hand side.

When a collision occurs, the name of the impacted neutral species is determined by comparing a new random number to a distribution weighted by collision probability per species. Likewise, the most likely process that occurred as a result of the collision is selected. ASPEN currently considers five processes: elastic collision, excitation (emission of a photon), ionization (ejection of an electron from the impacted neutral atom), charge exchange (capture of an electron from the impacted neutral), and electron stripping (ionization of a fast neutral hydrogen projectile). Each process causes the projectile to lose energy and scatter. ASPEN tracks where and how much energy is deposited by each collisional process, including the location and energy of any produced secondary electrons.

Following a collision, the particle's velocity is recalculated to account for lost energy and a new scattering direction before resuming tracing. The particle identity can also change, as the collision can change the state of the proton to a neutral hydrogen atom (charge exchange) and back (electron stripping). If the particle becomes a neutral hydrogen atom, the particle travels in a straight line unaffected by electromagnetic fields, which we trace using the same step length as a proton with the same energy.

A step length that accommodates gyromotion is not short enough to approximate distances between collisions in dense regions of an atmosphere. A 1 km step length is sufficient in the Martian atmosphere above an altitude of 300 km, since the highest neutral densities are $\sim 10^7 \text{ cm}^{-3}$ and the maximum cross section presented by atmospheric constituents is approximately 10^{-15} cm^2 , giving a distance of 1000 km before a single collision occurs. However, a particle traveling in the atmosphere at an altitude of 80 km encounters neutral densities approaching 10^{14} cm^{-3} , reducing the approximate distance between collisions to 10 cm. Using the larger distance as a step length undercounts collision but, since the simulation runtime is proportional to the number of steps taken because it solves the Lorentz force equation after each step, using the shorter step length increases simulation runtime by 10^5 . To account for both situations, we use an adaptive step length. If the cumulative collision likelihood increases too rapidly (e.g., over 20% in a single step), ASPEN reduces the step length by half and tries the step again. Likewise, if the cumulative collision likelihood increases too slowly, ASPEN doubles the step length up to the maximum step length required to simulate gyromotion.

2.2. Model Inputs

ASPEN requires four inputs. The first two are specific to a planetary atmosphere: neutral densities and magnetic fields. Electric fields can be optionally included. All should correspond to the same solar wind condition and orientation of Mars. The other two inputs are specific to the simulated projectile ion and the target neutral species: inelastic and elastic cross sections as a function of projectile energy and energy losses associated with each inelastic process, including secondary particle production for inelastic processes (eV).

2.2.1. Planetary Atmospheric Densities and Electromagnetic Fields

Number densities of each atmospheric constituent are either read from an altitude-varying profile or are approximated by a fixed value. Likewise, magnetic and electric fields are imported as an altitude-varying profile, globally varying profile, or a fixed value.

Planetary inputs can be toggled on or off to study specific cases. To examine particle motion in electric and magnetic fields ignoring atmospheric collisions (e.g., for verifying Lorentz trace accuracy in section 4.1), ASPEN can run in a trace-only mode that requires only electromagnetic fields. To study energy deposition in the absence of planetary electric and magnetic fields (e.g., for comparison to results in previously published studies on SEP energy deposition), ASPEN can run in a collision-only mode that only requires a density profile.

In this paper we use an altitude-varying density profile from MTGCM (Mars Thermosphere Global Circulation Model) of dayside Mars during solar minimum for the four most common species: CO₂, O, N₂, and CO [Bougher *et al.*, 2000, 2006]. We also use spatially varying 3-D magnetic and electric fields from the MF-MHD model [Dong *et al.*, 2014] including crustal fields with the strongest field region on the dayside of Mars during solar minimum. The MF-MHD simulation domain is a nonuniform spherical grid structure with a radial resolution varying from 5 km near the inner boundary to 1000 km near the outer boundary.

2.2.2. Collisional Cross Sections

ASPEN requires cross sections for each proton-impact process to model atmospheric effects. Because the maximum simulated energy is 5 MeV, relativistic collisional physics can be ignored. Protons with energies below 5 MeV undergo four collisional processes: excitation, ionization, charge transfer, and elastic collisions. From the ratio of the elastic cross section to the total cross section, we know that low-energy (~200 eV) protons undergo elastic collisions over 50% of the time. Protons with energies exceeding 200 eV are capable of imparting their energy to atomically interact with the impacted neutral molecule: capturing an electron to become a neutral (charge exchange), ripping an electron off the neutral (ionization), and emitting a photon (excitation). Protons that become neutral hydrogen are capable of the same processes except electron capture. Instead, the previously captured electron in neutral hydrogen can be ejected in a charge-stripping process.

ASPEN uses elastic collision, charge exchange, charge stripping, and ionization cross sections presented in Kallio and Barabash [2001], which were originally presented in Basu *et al.* [1987]. It also uses the excitation cross sections presented in Basu *et al.* [1987], which generalized all excitation processes under one cross section. As in Kallio and Barabash [2001], proton- and hydrogen-impact cross sections with carbon dioxide are approximated to be identical to proton- and hydrogen-impact cross sections with molecular oxygen. While several proton-impact cross sections with carbon dioxide have been discovered since the study done in Kallio and Barabash [2001], most cross sections for hydrogen-impact cross section with carbon dioxide remain unknown.

2.2.3. Collisional Energy Loss, Scattering, and Secondary Production

Protons lose energy when they impact neutral species. Energy loss in elastic processes is traditionally neglected because protons are light compared to the neutral molecules, as a proton has 2% the mass of a carbon dioxide atom. However, if a higher-energy proton undergoes an elastic collision, the energy imparted to heating is a fraction of that high energy. Likewise, particles are traditionally assumed to scatter forward. However, there is backscatter associated with elastic collisions. ASPEN therefore uses the scattering distribution presented in Kallio and Barabash [2001], based on modeled differential scattering cross sections from Noël and Pröls [1993], and calculates the energy lost using the conservation of energy and momentum equations for a two-body collision.

Energy losses associated with inelastic processes are documented in Basu *et al.* [1993]. To recap, energy lost in a charge exchange or excitation collision is fixed. In a charge exchange it is the difference between the impacted neutral ionization threshold and the proton ionization threshold. In an excitation, it is the upper threshold excitation energy of the impacted neutral. Energy lost in an electron ejection process is the sum of the ejected (secondary) energy and the energy cost to remove the electron. This can happen in two ways. The cost in an ionization collision is the ionization threshold of the impacted neutral. In a charge-stripping collision, the cost is the ionization threshold of the projectile neutral hydrogen. In both, the ejected secondary electron energy depends on projectile energy.

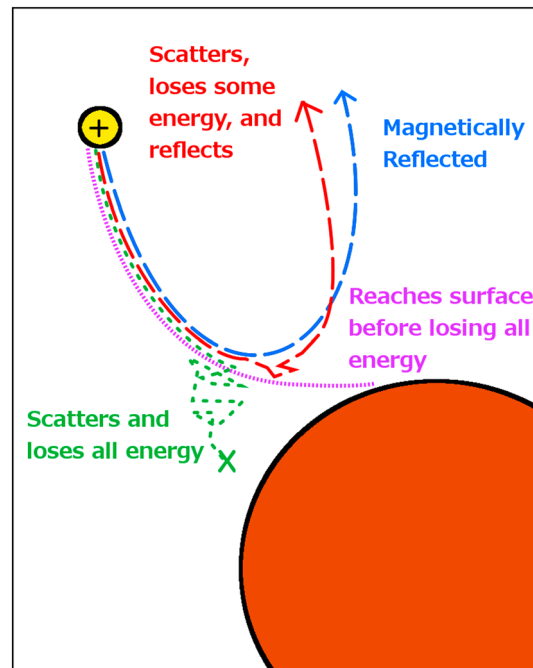


Figure 1. Schematic of proton transport in the ASPEN simulation. Particles are traced from 500 km and allowed to collide with neutral atmospheric species until they magnetically reflect without colliding, reflect after some collisions, collide until they have an energy below 10 eV and thermalize, or reach 70 km while still having an energy greater than 10 eV.

There are two approaches to predict secondary electron energies. In *Basu et al.* [1993] and *Kallio and Barabash* [2001], ionizations and electron-stripping collisions produce a secondary electron with a fixed energy depending on the primary energy (e.g., a 10 keV proton impacting N_2 in a charge-stripping collision produces a 6.4 eV electron). The fixed energy approach uses secondary electron energy data from *Basu et al.* [1993]. Alternatively, secondary electron production can be modeled using differential cross sections as in electron precipitation codes [e.g., *Lillis et al.*, 2008] allowing for the production of a range of secondary energies for a given projectile energy using random numbers. The random energy approach uses proton-impact ionization double differential cross sections with CO_2 , O_2 , O , and N_2 from *Rudd* [1988]. Unfortunately, there are no double differential cross sections for electron production in electron-stripping collisions.

ASPEN uses a fixed secondary approach for electron-stripping collisions and supports both fixed and double differential secondary production for ionization collisions. The approaches will be compared in section 5.2.

2.3. Model Outputs

ASPEN logs every simulated proton's energy and location when they exit the simulation, allowing us to verify the simulation logic by ensuring protons are not traced after physically leaving the simulation shell or falling below the energy threshold. The log is also useful to understand if and how injected protons deposit their energy. ASPEN particles "magnetically reflect" without depositing any energy, deposit their entire energy and "thermalize," or deposit a fraction of their energy before turning away and "scatter reflect" (Figure 1). Only particles with energies exceeding 5 MeV can reach the lower boundary of the simulation before depositing all their energy.

The primary output of ASPEN is a database containing detailed information on every simulated collision: latitude, longitude, and altitude of collision; species impacted; process occurred; whether the impacting particle was a proton or neutral hydrogen; energy deposited; secondary energy if secondary produced. There exists a single data structure for each incident SEP proton energy, location, and trajectory. The data structure contains the collisions for all simulated particles. As ASPEN is a Monte Carlo simulation, increasing the number of particles simulated improves model predictions. Optionally, ASPEN can be used to build a database containing each simulated particle's traced path, including positions and energies. These paths can be plotted to better understand particle behavior in the presence or absence of magnetic fields.

The data structures are aggregated over all simulated particles to predict observable properties. For example, CO_2^+ production rates for 1 keV solar wind protons can be plotted as a function of altitude. Furthermore, by integrating histograms of specific atmospheric processes over measured proton fluxes, ASPEN can predict rates of atmospheric effects caused by precipitating protons for any SEP event. This paper will focus on SEP-induced atmospheric ionization either in the absence of strong magnetic fields or nearby a specific crustal magnetic anomaly, including altitude profiles, geographical maps, and secondary electron spectra.

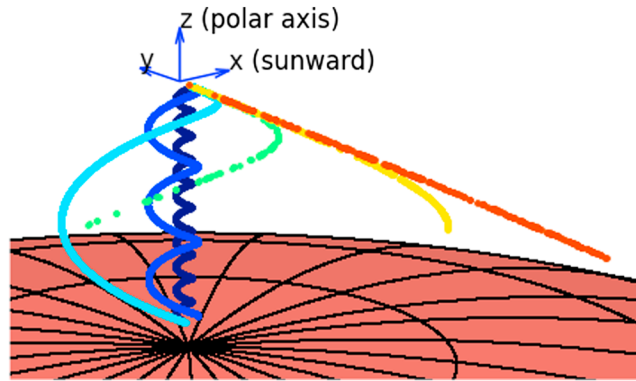


Figure 2. Traces of protons with different energies traversing an artificial 1 μ T z-directed field between altitudes 50 km and 300 km. Each particle is incident at particle zenith angle 60° (particle clock angle 0°) with energies 100 eV (dark blue), 1 keV (blue), 10 keV (cyan), 100 keV (green), 1 MeV (yellow), and 10 MeV (orange).

3. Verification and Validation

Because each procedure in the simulation code was written de novo, ASPEN was systematically tested to ensure the model predicts reasonable results. In this section, the verification of the Lorentz tracing and adaptive step algorithms will be described. Also described is the validation of collisional physics used in the model via comparison with two distinct atmospheric proton simulations. Finally, neutral heating rates calculated during a sample SEP event are compared to rates presented in *Leblanc et al. [2002]*.

3.1. Model Dynamics Verification

Charged particles gyrate around magnetic field lines with a fixed gyroradius in a uniform magnetic field. If a proton is traveling transverse and parallel to the magnetic field direction, it will travel in a helix. To verify that the Lorentz tracing algorithm predicted particle motion correctly, we used ASPEN's trace-only mode to generate the paths of protons with energies between 100 eV and 10 MeV traveling at a 60° angle to a 1 μ T vertical magnetic field (Figure 2). The predicted gyroradius of each particle matches the calculated gyroradius within an error of up to 1.6% at the lowest-energy simulated particle.

ASPEN's adaptive step algorithm accounts for short distances between collisions without the computational overhead of using the shortest distance between collisions as a fixed step length. To confirm that the adaptive step algorithm is as effective as a small fixed step, we disabled Lorentz tracing to simulate one thousand 1 keV incident protons using either four fixed step lengths between 1 m and 1 km or the adaptive algorithm (Figure 3). Using the adaptive algorithm predicts similar energy deposition to energy deposition predicted

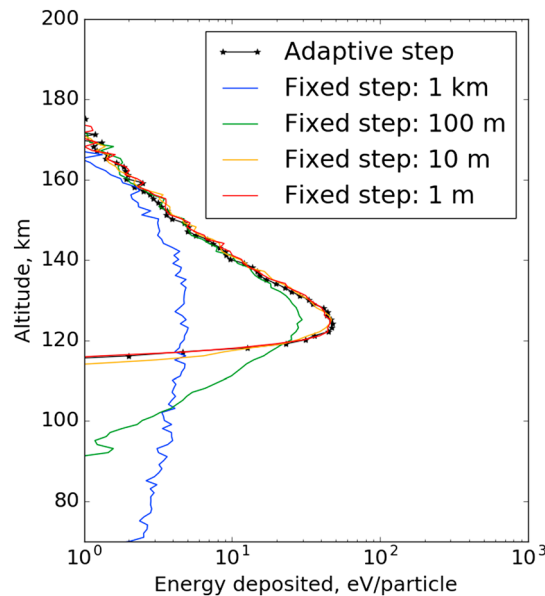


Figure 3. Comparison of energy deposition by a thousand 1 keV protons in the Martian atmosphere assuming no magnetic fields using different step length algorithms in the ASPEN simulation.

using a step length shorter than 50 m. The adaptive algorithm took 25 min to predict that the atmosphere absorbs 80% of the 1 keV proton beam's energy via collisional processes and scatters the rest, while using a 1 m fixed step length took 10 h to predict the same result.

We also observe that fixed step lengths longer than 10 m predict energy depositions that do not match either adaptive or short step length results. Using these step lengths predicts less energy deposition around the peak deposition altitude, as particles miss collisions occurring below 120 km and instead deposit energy far below the stopping altitude.

3.2. Collisional Physics Validation

The collisional physics in ASPEN were validated by running ASPEN in a

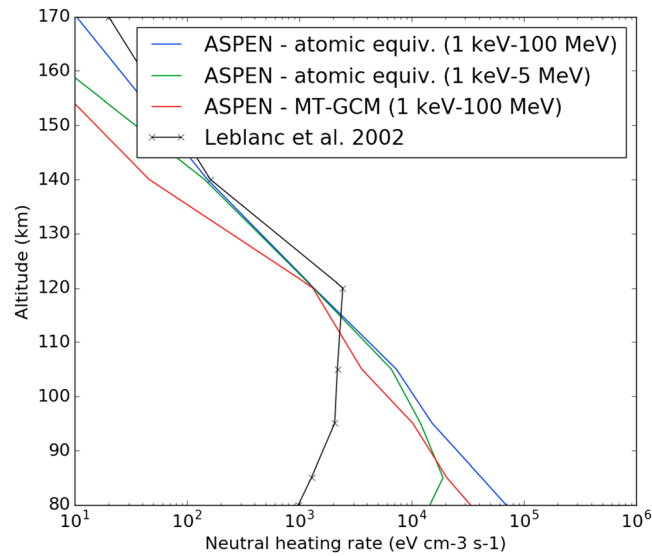


Figure 4. Comparison of neutral heating rates predicted by ASPEN and the SRIM results presented in *Leblanc et al.* [2002].

that 32% of the atoms were backscattered, which settles between SRIM's prediction of 10% and K&B's estimate of 58%.

We exclusively compare ASPEN and K&B predictions to validate energy deposition by ionization and excitation because SRIM does not distinguish inelastic processes. ASPEN predicts 26% of energy is deposited into ionization, agreeing with the 27% estimated from K&B. However, the energy deposited into excitation processes differs, as ASPEN predicts only 6% excitation unlike 30% in *Kallio and Barabash* [2001]. This is most likely because we approximated many different excitation mechanisms as a single process due to the lack of available excitation cross sections. Because we are focusing on ionization in this work and our results match the ionization results from previous work, this should not significantly impact the results in this paper.

3.3. SEP Event Comparison

ASPEN predicts ionization and heating rates during a SEP event. We can compare our rate calculation to the SEP proton heating rate presented in *Leblanc et al.* [2002]. The heating rate in *Leblanc et al.* [2002] was calculated by multiplying atmospheric densities in a thick slab by both SEP proton fluxes entering the exobase and energy deposited by protons in each slab. Using an atomic-equivalent atmosphere model, they approximated all atmospheric atoms as monatomic oxygen and determined the equivalent atmospheric density. Proton energy deposition was then determined using SRIM predictions of proton energy deposition in a column of monatomic oxygen.

Despite how ASPEN's operating range is limited to below 5 MeV due to lacking relativistic corrections and nuclear processes, extrapolating our nonrelativistic cross sections to 100 MeV enables ASPEN to predict a rate that can be compared to *Leblanc et al.* [2002]. Using the same SEP proton fluxes at 14 energies between 1 keV and 1 MeV as used in *Leblanc et al.* [2002], we calculate and compare heating rates using MTGCM dayside densities described in section 2.2.1 (plotted in green) and the same atomic-equivalent atmosphere densities used in *Leblanc et al.* [2002] (plotted in blue) (Figure 4). We also show heating rates using atomic-equivalent atmosphere densities integrated over the operating range of ASPEN (plotted in red).

ASPEN predicts up to 2 orders of magnitude more heating below 115 km and as low as 2 orders of magnitude less heating above 115 km. The missing relativistic processes cannot account for this, as we see the same trend for heating rates calculated using ASPEN operating range energies above 85 km. The effect is caused by particles in ASPEN depositing energy at lower altitudes than SRIM does. While *Leblanc et al.* [2002] predict a heating peak at 120 km caused by particles with energy between 0.5 and 10 keV, neither ASPEN prediction shows a peak. At 120 km, ASPEN predicts 20–500 keV proton fluxes deposit as much energy as 10 keV proton fluxes. These discrepancies can be owed to differences in cross sections, as our result is consistent with our

collision-only mode and comparing our predictions with reported results from two different models of light ion energy deposition in the Martian atmosphere: the stopping and range of ions in matter model (hereafter called "SRIM") [*Leblanc et al.*, 2002] and a model of fast neutral hydrogen atoms (hereafter called "K&B") [*Kallio and Barabash*, 2001].

Predictions from SRIM and K&B were previously compared in *Leblanc et al.* [2002] using the test case of incident 800 eV neutral hydrogen atoms. SRIM that predicted 16% of the energy was deposited into neutral heating, compared to 14% in K&B. ASPEN predicts that 13% of energy is deposited into heating, in close agreement with the prior two results. ASPEN also found

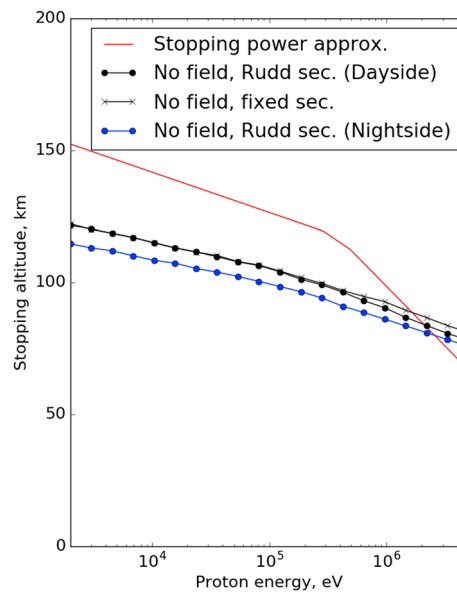


Figure 5. Comparison of stopping altitudes between a stopping power approximation (plotted in red) and the ASPEN simulation using dayside (plotted in black) and nightside (plotted in blue) atmospheric densities. ASPEN dayside stopping altitudes are also plotted for the Rudd secondary (circles) and fixed secondary models (crosses).

cross-section database. For example, using the ratio of the elastic cross section to the total cross section, the approximate probability of a 5 MeV proton elastically colliding with O is 4%. Since 5 MeV particles can have over 20,000 collisions before thermalizing, up to 1000 collisions can be elastic and heat the atmosphere. That is roughly the same number of elastic collisions that a 2 keV proton would have, as 2 keV protons can have 1500 collisions and a 70% chance of elastically scattering. However, the energy imparted by an elastic collision is proportional to the particle's incident energy. Thus, protons should impart energy to heating in amounts proportional to their energy, causing higher protons to heat the atmosphere more than low-energy protons and preventing the existence of a visible heating peak between 80 and 170 km.

We can also compare the fraction of energy imparted by heating to all altitudes between 80 and 170 km to the total energy imparted by the SEPs with energies between 1 keV and 100 MeV. ASPEN predicts 22% of the SEP energy flux is imparted to heating using MTGCM densities. Using the atomic-equivalent atmosphere shifts this heating efficiency to 31%, which is consistent with the heating efficiency of atomic oxygen. However, SRIM predicts only 2% of the input SEP energy is imparted to heating in this altitude range despite how SRIM predicts a heating efficiency of 16%. Because the energy cannot be imparted to other collisional processes, SRIM either underestimates heating above 80 km or predicts more heating energy is imparted below 80 km.

4. Proton Transport and Escape

Before examining the effects of a specific SEP event, we study proton transport and energy deposition as a function of proton energy. In the first subsection, we predict proton thermalization altitudes in the absence of magnetic fields and compare to previous model predictions. Next we investigate backscattering in a sample case of 10 keV protons. We then quantify rates of backscattering and thermalization for protons with energies between 2 keV and 5 MeV. Finally, we show energy deposition as a function of proton energy.

In the next two sections, we will compare ASPEN results from two distinct simulation runs. In both runs, a thousand protons with energies between 2 keV and 5 MeV are released from an altitude of 500 km traveling directly toward the dayside atmosphere of Mars during solar cycle minimum. In the “crustal field anomaly” run, particles are released over a crustal anomaly located at 50°S and 182°E. In the “absent magnetic fields” run, particles are released from the same location while magnetic fields are set to 0 nT. Secondary electrons produced by ionization have energies that are predicted using differential cross sections from *Rudd* [1988].

4.1. Thermalization Altitudes

Particles deposit more energy at lower altitudes because of increasing atmospheric densities. The maximum energy deposited is limited by the projectile's energy, causing protons with specific energies to be thermalized or “stopped” at a specific altitude. Prior studies have predicted stopping altitudes using the continuous slowing-down (CSD) approximation [*Henriksen*, 1978; *Sheel et al.*, 2012]. While ASPEN is a Monte Carlo model

that uses a random variable to calculate distances between individual collisions, the CSD approximation assumes particles with the same energy travel the same distance before thermalizing.

In Figure 5, we compare predictions of proton stopping altitude in the absence of magnetic fields. Stopping altitudes from ASPEN were taken by averaging the altitudes of protons with energies that fell below our 10 eV energy cutoff and are assumed to have thermalized in place. The CSD results used stopping ranges in carbon dioxide from proton stopping range tables provided by the National Institute of Standards and Technology [Berger *et al.*, 2005]. We solve for stopping altitudes by taking the atmosphere in hydrostatic equilibrium and balancing the gravitational force with atmospheric collisions, or $P(z) = P_0 e^{-z/H} = R(E)g$ for stopping range $R(E)$, gravitational constant g , scale height H , and surface pressure P_0 . As a first-order approximation, we used an isothermal carbon dioxide atmosphere with a scale height of 11.1 km.

In order to separate the influence of using different densities from the differences between the models, we gauge ASPEN's dependence on different neutral density profiles by determining stopping altitudes for both dayside solar minimum and nightside solar moderate MTGCM neutral density profiles. Higher stopping altitudes in a dayside atmosphere are expected, given higher atmospheric densities in the upper dayside atmosphere. We found that ASPEN stopping altitudes were 2–7 km higher in a dayside atmosphere than in a nightside atmosphere.

CSD-predicted stopping altitudes of protons with energies less than 2 MeV are up to 30 higher than ASPEN-predicted stopping altitudes. The difference is greatest for protons with energies below 300 keV. However, CSD also predicts lower stopping altitudes for protons with energy above 2 MeV. The CSD approximation predicts that 2 keV protons stop at 152 km and ASPEN predicts they stop at ~122 km, while 5 MeV protons stop at 67 km using the CSD approximation and at 78 km using ASPEN. These differences are greater than the variability observed between different atmospheres, meaning they could be caused by variation in cross sections or different approaches. The stopping power data used in the CSD approximation average over backscattered protons, which can decrease stopping range. In contrast, ASPEN determines stopping altitude by only averaging altitudes of thermalized particles. The difference between ASPEN and CSD results decreases for higher energies because the CSD approximation predicts less backscattering at high energies than ASPEN does.

4.2. Backscattering: Case Study

Not all protons that precipitate into an atmosphere are absorbed. Backscattering can attenuate and distribute the energy-depositing particle population. There are two causes of proton backscatter: atmospheric collisions and magnetic reflection. Atmospheric collisions stochastically turn particles back upward and away from the lower atmosphere. They are the only source of backscatter in the absence of magnetic fields. Magnetic reflection turns away protons in the upper atmosphere before they can deposit any energy. Atmospheric reflection and magnetic reflection can also act in tandem, allowing protons to deposit some energy in the atmosphere before being magnetically reflected.

Backscatter mechanisms are observable in traces of protons depositing energy (Figure 6). Figure 6a shows the paths of 10 identical 10 keV protons depositing energy in the absence of magnetic fields. Differences between the paths are caused by stochastic scattering events predicted by ASPEN. Six protons thermalize, losing all energy in the lower atmosphere. Four protons atmospherically scatter, losing substantial energy before reflecting with 10–50% of their initial energy. Atmospheric scattering is characterized by particles escaping with less than half of their initial energy.

Figure 6b shows the paths of ten 10 keV protons depositing energy into the atmosphere at a crustal anomaly located at 177°E and 7°S. Six protons magnetically reflect, taking the Lorentz path (the path of the same proton moving in without atmosphere, plotted in black) and escaping with 100% of their original energy. One proton atmospherically scatters exactly as in the previous case, escaping with less than 50% of its initial energy. Three protons have a different escape mechanism that is a combination of atmospheric scattering and magnetic reflection. Each scatters from 265 km, the altitude of closest approach in the Lorentz path (hereafter called the “magnetic reflection altitude”), and escapes with over 50% of their initial energy. Increased scattering at the magnetic reflection altitude is caused by particles moving parallel to the surface at this altitude, encountering the same neutral density for tens of kilometers which rapidly increasing the collision likelihood. The traces show that this mechanism distributes energy deposition over a greater area. Two

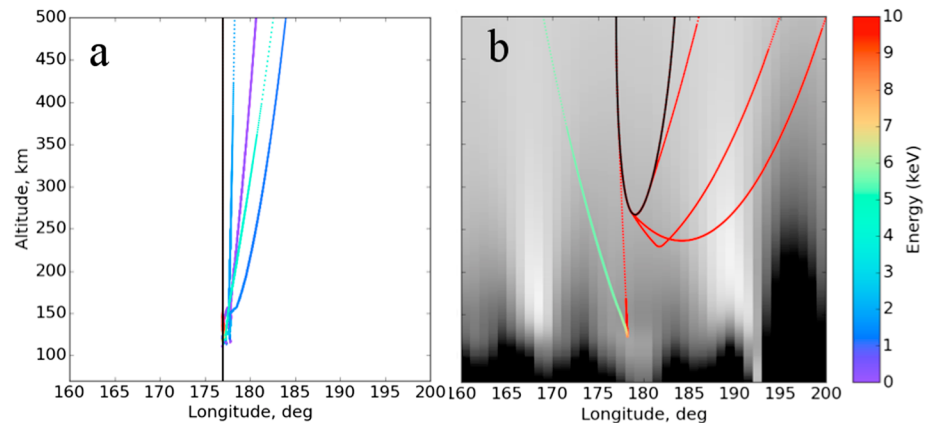


Figure 6. Traces of eleven 10 keV protons simulated in ASPEN entering at 177°E and 7°S injected directly ($\alpha = 0^\circ$) in a (a) purely collisional atmosphere with no magnetic fields and a (b) collisional atmosphere with magnetic and electric fields from MF-MHD. A noncollisional Lorentz path is plotted in black in both plots. Contours of the total magnetic field in the right figure are plotted in gray between 0 and 150 nT. Since the 10 traces are very similar, only ones that significantly scatter can be distinguished.

of the three traces show protons that become neutral hydrogen near the magnetic reflection altitude, causing them to travel in straight lines from the magnetic reflection altitude down to 240–250 km over 5–10°E from the launch location. These particles deposited energy along these paths before they were charge stripped, becoming again susceptible to magnetic fields, and then escaped.

4.3. Energy Dependence of Backscatter and Thermalization

Protons with energies less than 5 MeV either thermalize or backscatter. Atmospheric backscattering requires the occurrence of a nonforward scattering event, which is favored at different proton energies. Likewise, the likelihood of magnetic reflection depends on proton energy. Protons with lower energy are more susceptible to deflection by magnetic fields, meaning low-energy protons reflect higher in the atmosphere than high-energy protons. Magnetic reflection is also dependent on the magnetic topology of the region, but that is beyond the scope of this paper.

The energy dependence of backscattering (magnetically and atmospherically) is shown for absent magnetic fields and the studied crustal anomaly in Figure 7. In the absent magnetic fields case (Figure 7a), all protons deposit energy. Up to 75% of protons with energies below 80 keV deposit their entire energy in the atmosphere. However, between 100 keV and 1 MeV, the chance of thermalization drops to 50%. Protons with energies over 1.6 MeV are more likely to atmospherically backscatter.

The greater likelihood of higher-energy protons backscattering may seem counterintuitive. Due to the lack of angular cross-section data for inelastic processes, a key model assumption is that particles only change trajectory in elastic collisions. Elastic collisions only occur frequently for protons with energies below 500 eV. However, particles with energies over 1 MeV have over 10,000 collisions before thermalizing. Even a 5% chance of an elastic collision would cause over 500 elastic collisions, raising the likelihood of backscattering.

In the crustal field anomaly case (Figure 7b), protons with energy less than 400 keV are either magnetically reflected or backscattered. Over 95% of protons with energies below 10 keV will magnetically reflect without depositing any energy. The dominant proton backscattering process for energies below 119 keV is magnetic reflection without energy deposition. The dominant process switches to atmospheric scattering for protons with energies from 119 keV to up to 5 MeV. There are more backscattered 120–800 keV protons nearby a crustal anomaly than in the absence of magnetic fields. Most protons with these energies impart energy to the atmosphere before being magnetically reflected, like the three traces presented in section 5.2. These protons are counted as “scatter reflected” instead of “magnetically reflected” in Figure 7b because they can impart energy before reflecting. Protons with energies above 1 MeV are not as likely to atmospheric scatter as protons with energies between 100 keV and 1 MeV. Protons with energies greater than 300 keV have an over 5% chance of thermalizing, which increases to 50% for protons with energies between 1 MeV and 1.2 MeV.

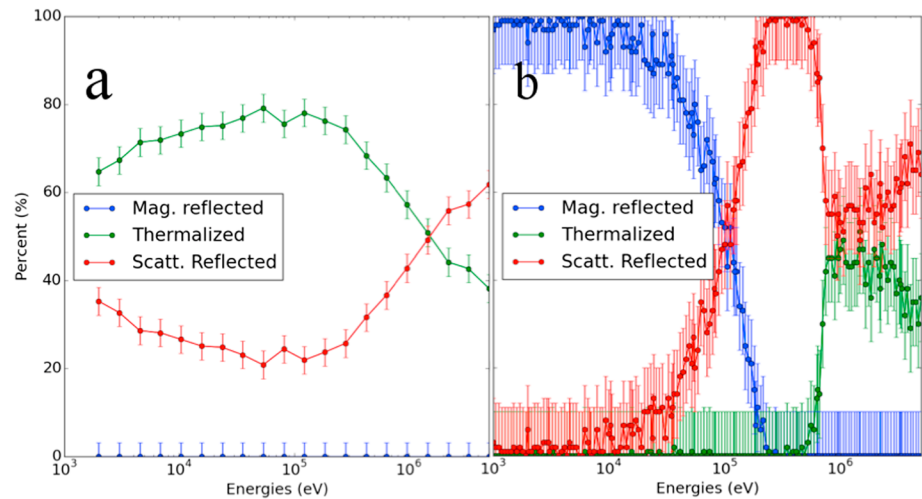


Figure 7. Proton escape as a function of energy for protons traversing through a collisional atmosphere (a) with no magnetic fields and (b) with magnetic and electric fields from MF-MHD. Monte Carlo error bars ($1/\sqrt{N}$) are shown for each energy where N is the number of simulated particles per energy (1000 in Figure 7a and 100 in Figure 7b).

Similar to how high-energy (>1 MeV) protons are mostly reflected in the absent fields case, the probability of thermalization plummets for protons with energies above 2 MeV.

4.4. Energy Dependence of Altitude-Varying Energy Deposition

The previous sections have considered energy deposition by thermalization and backscattering mechanisms in isolation. In this subsection, total energy deposition is aggregated regardless of mechanism, both overall and as a function of altitude, to study energy absorption as a function of proton energy and magnetic fields.

In the absence of magnetic fields, protons with energies below 454 keV deposit 80–91% of their energy in the atmosphere. Energy deposition by protons with energies above 454 keV steadily declines, as 963 keV protons deposit 70% and 5 MeV protons deposit only 51% of their energy. The lowered energy deposition coincides with increased elastic scattering.

Nearby a crustal field anomaly, protons with energies below 454 keV only deposit as much as 1% of their energy. Opposite to the absent fields case, energy deposited by protons with energies above 454 keV dramatically increases with primary energy. The 1.5 MeV protons deposit approximately 60% of their energy. Percent energy deposition slowly decreases for protons with energies above 2.3 MeV, with 5 MeV protons depositing 51% of their energy. In net, protons with energies below 1 MeV deposit nearly no energy in the vicinity of a crustal anomaly, while protons with energies above 1 MeV deposit as much energy near a crustal anomaly as they would in the absence of magnetic fields.

Regardless of the presence of magnetic fields, the net energy deposition aggregated by altitude between 70 and 300 km is inversely proportional to the altitude, smoothly increasing as altitude decreases (Figure 8). Higher-energy protons deposit more energy at lower altitudes.

Protons deposit 99.94% of their energy below 150 km in the absence of fields (Figure 8a). The average maximum deposited energy above 150 km is 1.7 eV/km. Occasionally, energies over 50 eV/km are deposited above 150 km, seen as speckles in Figure 8a. These seemingly anomalous large energy depositions at higher altitudes are caused by elastic collisions. Although elastic collisions are infrequent for particles with energies greater than 500 eV, the energy lost in a single elastic collision is proportional to the proton's initial energy at the time of scatter.

The energy deposition distribution by protons near a crustal field anomaly shows overall much less energy deposition compared to the absent fields case (Figure 8b). The most notable feature of Figure 8b is that protons with energies between 50 keV and 800 keV deposit energy in two regions: in a narrow altitude range around the proton stopping altitudes in the absence of magnetic fields (plotted in red) and at the magnetic reflection altitude (plotted in black). More energy is deposited at the magnetic reflection altitude than

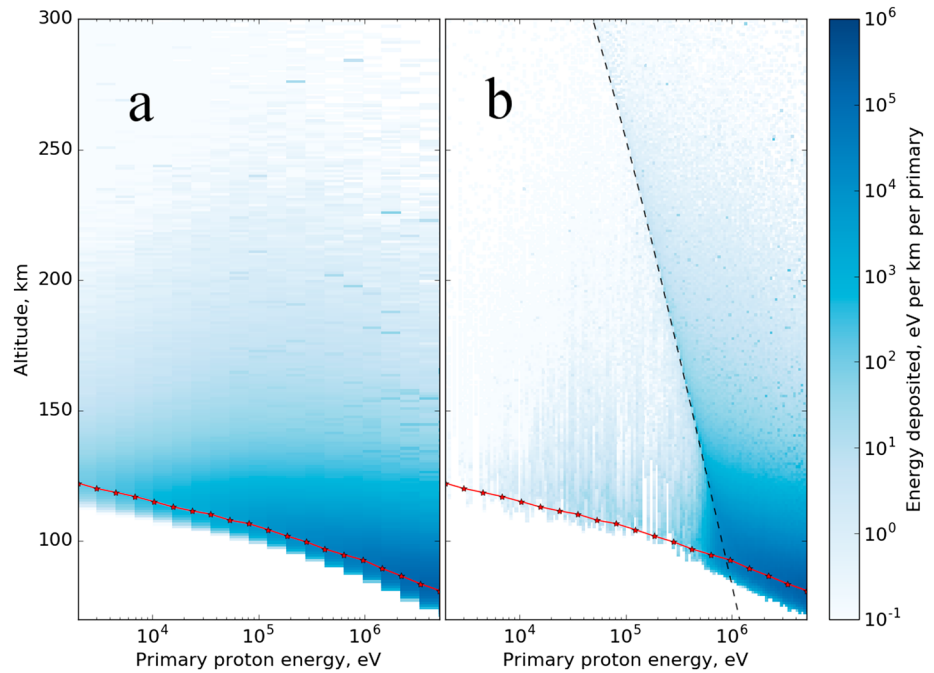


Figure 8. Energy deposited per primary by a protons with energies between 2 keV and 5 MeV injected in a (a) purely collisional atmosphere with no magnetic fields and a (b) collisional atmosphere with magnetic and electric fields from MF-MHD. The altitude of magnetic reflection is plotted in black, and the stopping altitude in a purely collisional atmosphere is plotted in red.

between the stopping altitude and magnetic reflection altitude. This is because the particle is traveling laterally, so the path length in that altitude bin is higher, increasing the energy deposited. When the altitude of magnetic reflection falls below 110 km (for 700 keV), the energy deposition profile is similar to the absent fields case except with a slightly higher altitude of maximum energy deposition. For example, 1.5 MeV protons deposit the maximum amount of energy at 87 km near a crustal field anomaly compared to 85 km in the absence of magnetic fields.

Energy deposition in the lower atmosphere by protons with low energies (<500 keV) is much less in crustal fields than in the absence of magnetic fields. These protons must be both elastically scattered and charge stripped at the magnetic reflection altitude in order to deposit energy below 150 km. Protons with energies below 100 keV deposit ~1 eV/km below 150 km, compared to 190 eV/km in the absence of magnetic fields.

5. SEP Event Predictions

Using the data sets generated in the previous section, we can determine rates of ionization near a crustal anomaly and in the absence of magnetic fields. For the flux $F(E)$ and collision rate $R(E, a)$ at altitude a for SEP protons with energy E , the process rate during a SEP event is

$$I(a) = \int_{E_i}^{E_f} F(E)R(E, a)dE$$

Following the method for determining rates in *Leblanc et al.* [2002] by using 14 energies between 1 keV and 100 MeV, we use 1 keV as our lower energy bound. The 5 MeV is our upper energy bound, as 5 MeV is the highest-energy ASPEN can simulate. Our results are relatively accurate from 300 km to 70 km. We use fluxes from the peak SEP spectrum measured on 29 October 2003 5:59 (Figure 9) by the Electrons, Protons, and Alpha Monitor (EPAM) on the ACE spacecraft, located at 1 AU [Chiu et al., 1998]. This event, colloquially known as the “Halloween storm,” has been previously used as a proxy for predicting SEP effects at Mars [Lillis et al., 2012].

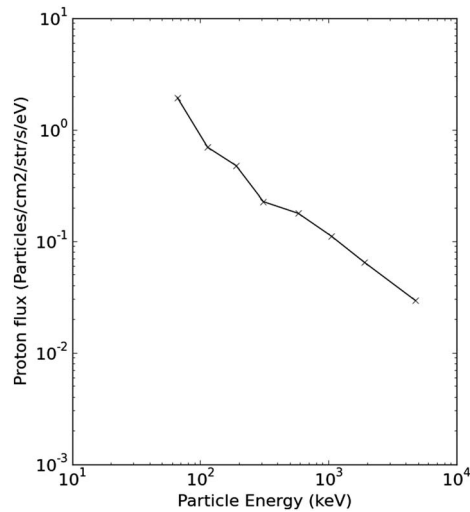


Figure 9. Spectrum of peak spectrum during the 28 October 2003 SEP event as measured by Solar Wind Electron, Proton, and Alpha Monitor.

is expected, as crustal fields attenuate SEP penetration below 500 keV. Peak ionization is $12,552 \text{ cm}^{-3} \text{ s}^{-1}$ at 83 km, which is an $\sim 15\%$ reduction compared to the absent fields case. There is no comparable ionization bump at 115 km nearby the crustal anomaly.

We determined volume rates of ionization in the vicinity of proton injection location (Figure 11). In the absence of magnetic fields, the maximum ionization rate is $697 \text{ cm}^{-3} \text{ s}^{-1}$ per $^\circ\text{N}$ per $^\circ\text{E}$, located at the same geographic location protons were injected at (marked with a star, Figure 11a). Ionization is overall radially symmetric across the region, spreading in 5° in each direction.

Ionization volume rates near a crustal anomaly are not symmetric at all (Figure 11b). Volume rates are plotted below contours representing horizontal magnetic fields, colored according to the radial component (blue is below -40 nT and red is above 40 nT). The maximum ionization rate is $481 \text{ cm}^{-3} \text{ s}^{-1}$ per $^\circ\text{N}$ per $^\circ\text{E}$ at 50°S 180°E , approximately 2°E from where protons were injected. Ionization over $50 \text{ cm}^{-3} \text{ s}^{-1}$ per $^\circ\text{N}$ per $^\circ\text{E}$ spreads northwest of the injection location and ionization below $50 \text{ cm}^{-3} \text{ s}^{-1}$ per $^\circ\text{N}$ per $^\circ\text{E}$ largely occurs southeast.

The northwest ionization follows the Lorentz trajectory of energetic particles.

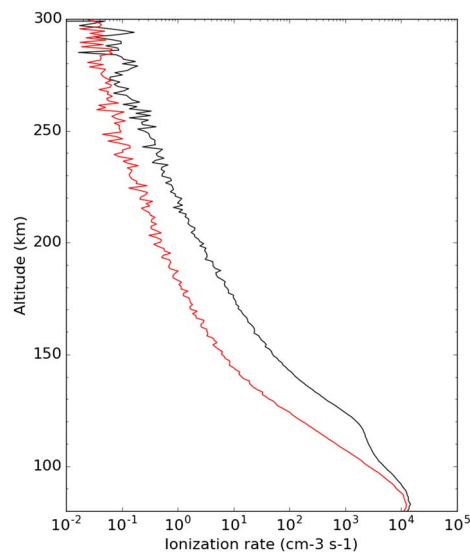


Figure 10. Altitude profiles of ionization rate during the 28 October 2003 SEP event using a population of protons injected at 50°S and 182°E on the dayside over nonmagnetized crust (black) and a crustal anomaly (red).

5.1. Crustal Field Influences

Predicted ionization rates near a crustal field anomaly and in the absence of magnetic fields during the EPAM event are shown in Figure 10. In the absence of magnetic fields (black line), the peak ionization above 70 km is $14,853 \text{ cm}^{-3} \text{ s}^{-1}$ at 83 km. There is a slight increase in ionization between 105 and 132 km that peaks at $\sim 2000 \text{ cm}^{-3} \text{ s}^{-1}$ at 115 km, which is caused by the slightly higher fluxes of 100–300 keV particles measured by EPAM. Total ionization nearby a crustal field anomaly (red line) is 68.3% of ionization in the absence of magnetic fields. Such a decrease

5.2. Secondary Electron Production

ASPEN logs the energy of any produced secondaries from ionization and charge stripping. Secondary energies are aggregated to predict the spectrum of secondary electrons at each altitude. Similar to the calculation of ionization rate, each spectrum per altitude is integrated over the EPAM fluxes to predict an altitude profile of secondary electron production during an event.

As described in section 2.2.3, there are two approaches to predicting secondary electron energy in a

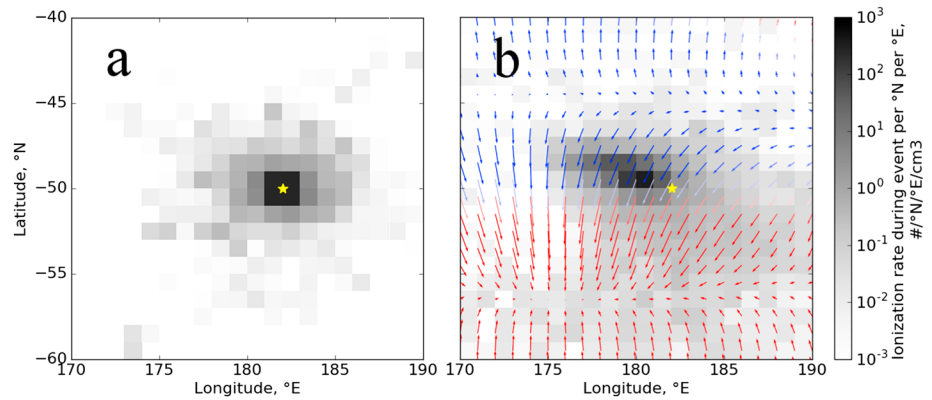


Figure 11. Map of SEP-induced ionization volume rate for SEPs directed at the anomaly located at 50°S and 182°E if magnetic fields in the simulation are toggled (a) off or (b) on. The star marks where protons are injected. The contours mark horizontal magnetic fields at an altitude of 400 km where the color indicates the radial component of the magnetic field where red is +40 nT and blue is -40 nT.

collision: using a random secondary energy from a double differential cross section or using a fixed secondary energy from extrapolating an existing data set. Both approaches produce near-identical ionization rates down to an altitude of 95 km. Below an altitude of 95 km, the fixed secondary energy approach predicts 28% less ionization than the Rudd secondary energy. The discrepancy is because the fixed secondary energy extrapolation predicts substantially higher secondary energies for >1 MeV protons than the Rudd secondary energy method, causing protons to lose energy quicker and ionize less frequently. Since the Rudd secondary energy approach is based on an empirically verified double differential cross-section expression, we consider it more realistic than the fixed secondary energy approach. We will continue to use this approach in the future.

Altitude profiles of secondary electron spectra were determined in the absence of magnetic fields using fixed (Figure 12a) and random secondary energy approaches (Figure 12b). The fixed secondary energy model

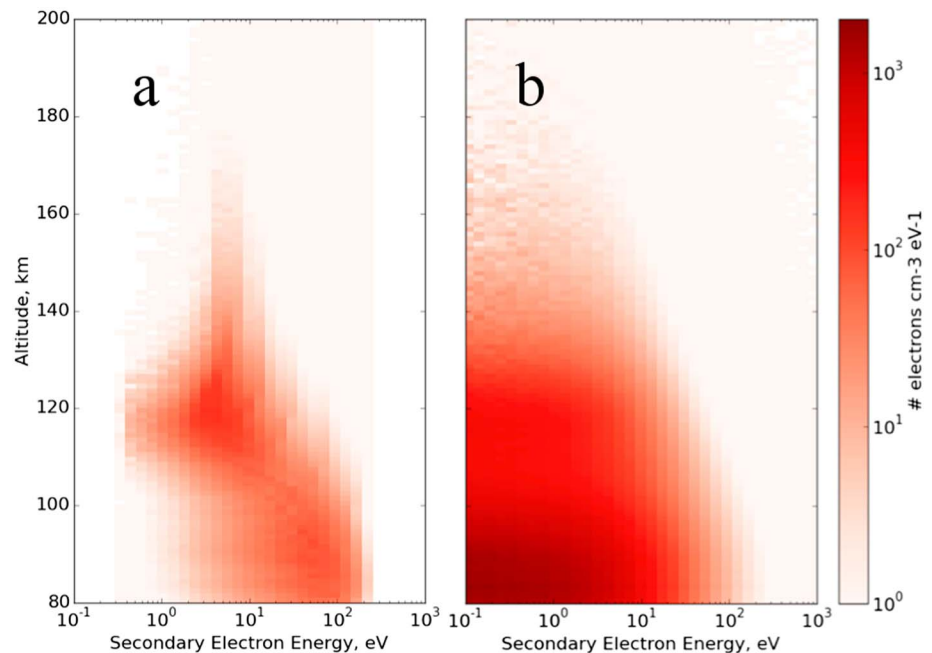


Figure 12. Spectrum of electrons produced by SEP proton-impact ionization over unmagnetized crust using a (a) fixed secondary electron energy model and a (b) random secondary electron energy model.

predicts that most secondaries have energies between 10 eV and 200 eV. The random secondary energy model predicts production of many more secondary electrons with energies distributed between 0.01 eV and 100 eV. The models have different implications for SEP-produced upward electron fluxes. The production rate of 110 eV electrons at 150 km is $13 \text{ el cm}^{-3} \text{ s}^{-1} \text{ keV}^{-1}$ in the fixed energy model and $4 \text{ el cm}^{-3} \text{ s}^{-1} \text{ keV}^{-1}$ in the random energy model.

6. Conclusion

We have validated and demonstrated the application of a novel proton transport and collisional physics model. The ASPEN model predicts atmospheric effects by SEP precipitation by including ionization and heating. It uses an adaptive step length algorithm, allowing accurate predictions while running 20 times faster than if we were to use the shortest step length. We compared heating rates from the ASPEN model to published results from previous models, finding that ASPEN predicted significantly greater heating than the model presented in *Leblanc et al.* [2002] and that protons deposited their energy up to 20 km lower in altitude than for models using a conventional continuous slowing-down approximation.

Unlike many other simulations of SEP precipitation into planetary atmospheres, ASPEN accounts for charged particle motion in spatially varying magnetic fields. We used ASPEN to study the effects of a specific anomaly located at 50°S and 182°E on atmospheric ionization. Early results suggest that SEP protons deposit a substantial amount of energy in the atmosphere above the crustal field anomalies. However, proximity to crustal fields can reduce overall atmospheric ionization by ~30%. Atmospheric ionization near a crustal anomaly spreads over a wider geographic area than atmospheric ionization in the absence of magnetic fields. The distribution of atmospheric ionization occurs along an axis corresponding to the Lorentz trajectories of SEP protons.

We also compared ASPEN secondary electron production predictions in negligible magnetic fields using two different methodologies: randomly selecting a secondary energy using the double differential cross section or extrapolating previously determined secondary energies to calculate a fixed secondary energy. Overall ionization predicted by both methods is similar above an altitude of 95 km. We determined production rates of superthermal electrons (~110 eV) from proton-impact ionization at the limiting altitude where electrons preferentially thermalize instead of backscattering (150 km) [*Lillis et al.*, 2012]. Electron production rates predicted using the random secondary energy model are half that from using the fixed secondary energy model. These electron populations can be modeled using electron transport codes to see if they explain the increased upward electron fluxes observed by MGS.

We demonstrated that SEP protons cause substantially less ionization if they are incident on a specific location in close proximity to a crustal field anomaly. Future work will include an investigation of how crustal anomalies influence ionization from SEP protons precipitating globally. Precipitating low-energy SEPs (~10 keV) can be magnetically reflected from between 18 and 50% of the atmospheric area presented by the dayside southern hemisphere if the crustal fields are on the dayside. We intend to determine and incorporate the SEP flux dependence on solar zenith angle in order to study SEP ionization over crustal anomaly regions, which eventually will be expanded into global maps. The progression of atmospheric ionization during a SEP event can also be tracked using data from the SEP instrument on MAVEN, allowing for estimates of time dependent and total ionization and heating during an event.

Finally, the ASPEN model has broad applications for future use and could be a community-modeling tool. For example, the radiation environment at Mars is extremely harsh. The MARIE (MArtian Radlation Experiment) instrument on board Mars Odyssey was intended to characterize the environment but malfunctioned following a strong SEP event [*Luhmann et al.*, 2007]. The ASPEN open-source modules provide the opportunity for independent research development for near-Mars SEP flux calculations, auroral predictions, and surface radiation modeling.

References

- Acuña, M. H., et al. (2001), The magnetic field of Mars: Summary results from the aerobraking and mapping orbits, *J. Geophys. Res.*, *106*, 23,403–23,417, doi:10.1029/2000JE001404.
- Basu, B., J. R. Jasperse, R. M. Robinson, R. R. Vondrak, and D. S. Evans (1987), Linear transport theory of auroral proton precipitation: A comparison with observations, *J. Geophys. Res.*, *92*, 5920–5932, doi:10.1029/JA092iA06p05920.

Acknowledgments

This research was supported by the MAVEN project (supported by NASA through the Mars Exploration Program), NASA PATM grant NNX11AD81G and NASA MFRP grant NNX13AG52G. C.F. Dong is currently supported by the NASA Living with a Star Jack Eddy Postdoctoral Fellowship Program, administered by the University Corporation for Atmospheric Research. The source code and input files necessary to reproduce the ASPEN model results analyzed in this work are available from the authors upon request (rebecca.jolitz@colorado.edu).

- Basu, B., J. R. Jasperse, D. J. Strickland, and R. E. Daniell Jr. (1993), Transport-theoretic model for the electron-proton-hydrogen atom aurora. 1: Theory, *J. Geophys. Res.*, *98*, 21,517–21,532, doi:10.1029/93JA01646.
- Berger, M. J., J. S. Coursey, M. A. Zucker, and J. Chang (2005), ESTAR, PSTAR, and ASTAR: Computer Programs for Calculating Stopping-Power and Range Tables for Electrons, Protons, and Helium Ions (version 1.2.3), Natl. Instit. of Stand. and Technol., Gaithersburg, Md. [Available at <http://physics.nist.gov/star/>]
- Bougher, S. W., S. Engel, R. G. Roble, and B. Foster (2000), Comparative terrestrial planet thermospheres 3. Solar cycle variation of global structure and winds at solstices, *J. Geophys. Res.*, *105*, 17,669–17,692, doi:10.1029/1999JE001232.
- Bougher, S. W., J. M. Bell, J. R. Murphy, M. A. Lopez-Valverde, and P. G. Withers (2006), Polar warming in the Mars thermosphere: Seasonal variations owing to changing insolation and dust distributions, *Geophys. Res. Lett.*, *33*, L02203, doi:10.1029/2005GL024059.
- Chiu, M. C., et al. (1998), ACE spacecraft, *Space Sci. Rev.*, *86*, 257.
- Damiani, A., M. Storini, M. L. Santee, and S. Wang (2010), The hydroxyl radical as an indicator of SEP fluxes in the high-latitude terrestrial atmosphere, *Adv. Space Res.*, *46*, 1225–1235, doi:10.1016/j.asr.2010.06.022.
- Delory, G. T., J. G. Luhmann, D. Brain, R. J. Lillis, D. L. Mitchell, R. A. Mewaldt, and T. V. Falkenberg (2012), Energetic particles detected by the Electron Reflectometer instrument on the Mars Global Surveyor, 1999–2006, *Space Weather*, *10*, S06003, doi:10.1029/2012SW000781.
- Desorgher, L., E. O. Flückiger, M. Gurtner, M. R. Moser, and R. Bütikofer (2005), ATMOCOSMICS: A GEANT4 code for computing the interaction of cosmic rays with the Earth's atmosphere, *Int. J. Mod. Phys. A*, *20*, 6802–6804.
- Dong, C. F., S. W. Bougher, Y. J. Ma, G. Toth, A. F. Nagy, and D. Najib (2014), Solar wind interaction with Mars upper atmosphere: Results from the one-way coupling between the multi-fluid MHD model and the M-TGCM model, *Geophys. Res. Lett.*, *41*, 2708–2715, doi:10.1002/2014GL059515.
- Espley, J. R., W. M. Farrell, D. A. Brain, D. D. Morgan, B. Cantor, J. J. Plaut, M. H. Acuña, and G. Picardi (2007), Absorption of MARSIS radar signals: Solar energetic particles and the daytime ionosphere, *Geophys. Res. Lett.*, *34*, L09101, doi:10.1029/2006GL028829.
- Futaana, Y., et al. (2008), Mars Express and Venus Express multi-point observation's of geoeffective solar flare events in December 2006, *Planet. Space Sci.*, *56*(6), 873–880, doi:10.1029/2012SW000781.
- Gronoff, G., C. Mertens, J. Lilensten, L. Desorgher, E. Flückiger, and P. Velinov (2011), Ionization processes in the atmosphere of Titan. III. Ionization by high-Z nuclei cosmic rays, *Astron. Astrophys.*, *529*, A143, doi:10.1051/0004-6361/201015675.
- Gronoff, G., R. B. Norman, and C. J. Mertens (2015), Computation of cosmic ray ionization and dose at Mars. I: A comparison of HZETRN and Planetocosmics for proton and alpha particles, *Adv. Space Res.*, *55*, 1799–1805.
- Henriksen, K. (1978), Variations of proton energy and pitch-angle spectra in the upper atmosphere, *J. Atmos. Terr. Phys.*, *41*, 633.
- Kallio, E., and S. Barabash (2001), Atmospheric effects of precipitating energetic hydrogen atoms on the Martian atmosphere, *J. Geophys. Res.*, *106*, 165–178, doi:10.1029/2000JA002003.
- Kokorowski, M., et al. (2006), Rapid fluctuations of stratospheric electric field following a solar energetic particle event, *Geophys. Res. Lett.*, *33*, L20105, doi:10.1029/2006GL027718.
- Leblanc, F., J. G. Luhmann, R. E. Johnson, and E. Chassefiere (2002), Some expected impacts of a solar energetic particle event at Mars, *J. Geophys. Res.*, *107*(A5), 1058, doi:10.1029/2001JA900178.
- Lee, C. O., et al. (2017), MAVEN observations of the solar cycle 24 space weather conditions at Mars, *J. Geophys. Res. Space Physics*, *122*, 2768–2794, doi:10.1002/2016JA023495.
- Lillis, R. J., D. L. Mitchell, R. P. Lin, and M. H. Acuña (2008), Electron reflectometry in the Martian atmosphere, *Icarus*, *194*, 544–561, doi:10.1016/j.icarus.2007.09.030.
- Lillis, R. J., D. A. Brain, G. T. Delory, D. L. Mitchell, J. G. Luhmann, and R. P. Lin (2012), Evidence for superthermal secondary electrons produced by SEP ionization in the Martian atmosphere, *J. Geophys. Res.*, *117*, E03004, doi:10.1029/2011JE003932.
- Lillis, R. J., C. O. Lee, D. Larson, J. G. Luhmann, J. S. Halekas, J. E. Connerney, and B. M. Jakosky (2016), Shadowing and anisotropy of solar energetic ions at Mars measured by MAVEN during the March 2015 solar storm, *J. Geophys. Res. Space Physics*, *121*, 2818–2829, doi:10.1002/2015JA022327.
- Luhmann, J. G., C. Zeitlin, R. Turner, D. A. Brain, G. Delory, J. G. Lyon, and W. Boynton (2007), Solar energetic particles in near-Mars space, *J. Geophys. Res.*, *112*, E10001, doi:10.1029/2006JE002886.
- McKenna-Lawlor, S., V. V. Afonin, E. Kirsch, K. Schwingenschuh, J. A. Slavin, and J. G. Trotignon (1998), An overview of energetic particles (from 55 keV to >30 MeV) recorded in the close Martian environment and their energization in local and external processes, *Planet. Space Sci.*, *46*, 83–102.
- Mironova, I. A. and I. G. Usoskin (2014), Possible effect of strong solar energetic particle events on polar stratospheric aerosol: A summary of observational results, *Environ. Res. Lett.*, *9*(1), 015002, doi:10.1088/1748-9326/9/1/015002.
- Mironova, I. A., K. L. Aplin, F. Arnold, G. A. Bazilevskaya, R. G. Harrison, A. A. Krivolutsky, K. A. Nicoll, E. V. Rozanov, E. Turunen, and I. G. Usoskin (2015), Energetic particle influence on the Earth's atmosphere, *Space Sci. Rev.*, *194*, 1, doi:10.1007/s11214-015-0185-4.
- Moore, T. E., W. K. Peterson, C. T. Russell, M. O. Chandler, M. R. Collier, H. L. Collin, P. D. Craven, R. Fitzenreiter, B. L. Giles, and C. J. Pollock (1999), Ionospheric mass ejection in response to a coronal mass ejection, *Geophys. Res. Lett.*, *26*, 2339–2342, doi:10.1029/1999GL900456.
- Morgan, D. D., D. A. Gurnett, D. L. Kirchner, J. L. Fox, E. Nielsen, and J. J. Plaut (2008), Variation of the martian ionospheric electron density from Mars Express radar soundings, *J. Geophys. Res.*, *113*, A09303, doi:10.1029/2008JA013313.
- Norman, R. B., T. C. Slaba, and S. R. Blattnig (2013), An extension of HZETRN for cosmic ray initiated electromagnetic cascades, *Adv. Space Res.*, *51*, 2251–2260.
- Noël, S., and G. W. Prölss (1993), Heating and radiation production by neutralized ring current particles, *J. Geophys. Res.*, *98*, 17,317–17,325, doi:10.1029/93JA01500.
- Rudd, M. E. (1988), Differential cross sections for secondary electron production by proton impact, *Phys. Rev. A.*, *38*(12), 6129–6137.
- Schneider, N. M., et al. (2015), Discovery of diffuse aurora on Mars, *Science*, *350*, doi:10.1126/science.aad0313.
- Sheel, V., S. A. Haider, P. Withers, K. Kozarev, I. Jun, S. Kang, G. Gronoff, and C. Simon Wedlund (2012), Numerical simulation of the effects of a solar energetic particle event on the ionosphere of Mars, *J. Geophys. Res.*, *117*, A05312, doi:10.1029/2011JA017455.
- Usoskin, I. G., L. Desorgher, P. Velinov, M. Storini, E. O. Flückiger, R. Bütikofer, and G. A. Kovaltsov (2009), Ionization of the Earth's atmosphere by solar and galactic cosmic rays, *Acta Geophys.*, *57*, 88–101, doi:10.2478/s11600-008-0019-9.
- Ulusen, D., D. A. Brain, J. G. Luhmann, and D. L. Mitchell (2012), Investigation of Mars' ionospheric response to solar energetic particle events, *J. Geophys. Res.*, *117*, A12306, doi:10.1029/2012JA017671.